Received 18 January 2023; revised 3 March 2023; accepted 16 March 2023. Date of publication 27 March 2023; date of current version 14 April 2023.

Digital Object Identifier 10.1109/OJAP.2023.3261903

Angle-Dependent Synthesis Method for Holographic Multi-Feed Antennas

THOMAS FREY (Graduate Student Member, IEEE), MAXIMILIAN DÖRING, NICO RIESE (Graduate Student Member, IEEE), CHRISTIAN WALDSCHMIDT (Fellow, IEEE), AND TOBIAS CHALOUN (Member, IEEE)

Institute of Microwave Engineering, University of Ulm, 89081 Ulm, Germany

CORRESPONDING AUTHOR: T. FREY (e-mail: thomas.frey@uni-ulm.de)

This work was supported in part by the German Federal Ministry of Education and Research (BMBF) and the Federal States of Germany Grant "Innovative Hochschule" (FKZ) under Grant 03IHS024D, and in part by the German Research Foundation under Grant CH 2226/4-1.

ABSTRACT A novel synthesis method for holographic multi-feed antennas is presented to combine all sub-holograms into an angle-dependent shared holographic aperture. In order to find the global error minimum between the shared holographic aperture and all ideal sub-holograms, a non-pixel-based genetic optimization is used. For a more accurately implementation of the analytical impedance tensor an eigenvector approach taking all tensor components into account is introduced. The optimized holographic antenna has four feeds for an exemplary integration into a 2D-monopulse radar system and is realized on a fused silica wafer due to its lower loss at millimeter-wave frequencies compared to Teflon-based materials. The antenna prototype provides a measured gain of 23 dBi, a polarization purity of 26 dB and a side-lobe level of 20 dB for feed 1, 2 and 4 is reached across 76 GHz−81 GHz. The S-parameters are measured from 60 GHz to 90 GHz, and a reflection coefficient of −14 dB and an inter-port coupling <−38 dB are achieved. The measured 2D-monopulse patterns provide a FOV of 10°, the sum beam has a gain of 26 dBi leading to an aperture efficiency of 45 % and the differential beams show a null depth of 30 dB.

INDEX TERMS Holographic antenna, metasurface antenna, multi-feed antenna, multi-beam antenna, surface wave, leaky wave, monopulse radar, glass technology.

I. INTRODUCTION

HOLOGRAPHIC antennas are gaining an increasing interest in the mm-wave application area, e.g., for the sensor and communication scope, since they allow for a highly flexible control of the aperture field concerning amplitude and phase distribution and also regarding the polarization of the electromagnetic far field [1], [2], [3], [4], [5]. This can be achieved by a modulated impedance surface consisting of a dense periodic structure of several thousands of sub-wavelength discontinuities. These are placed on an electrically thin grounded dielectric slab, which is described by the impedance boundary condition (IBC) [6]. The IBC enables the control of the propagation direction of a guided surface wave (SW) and also their transformation into higher order Floquet modes. The holographic antenna provides a very low building depth, typically small compared to the wavelength, and this promotes the integration of holographic antennas into a package [7], [8], [9], [10], [11]. The antenna-in-package (AiP) approach provides a scalable aperture size and minimizes the losses significantly at mm-wave frequencies compared to a conventional planar distribution network [12], [13]. Hence, a high-gain holographic AiP with a desired far field pattern can be achieved.

In [14], [15], [16], [17], [18] an isotropic IBC is used to control the propagation direction of a non-radiating SW mode. The SW excitation is provided by a surface wave launcher (SWL) which can be implemented by a circular patch. By introducing a modulation period, the SW is transformed into higher order modes, described by the Floquet series [19]. Thus, the interaction of a guided SW with the modulated impedance surface implies that the $(-1, -1)$ Floquet mode enters the visible region and thus becomes a continuously radiating leaky wave (LW) [20]. In [21], [22] the modulated impedance surface is arranged in a spiral shape in order to

generate a circularly polarized LW radiation, but the isotropic IBC results in a poor polarization purity.

Modulated impedance surfaces based on an anisotropic IBC approach are described by impedance tensors to enhance the quality of the circularly polarized LW radiation [23]. In this way, an increased polarization purity and antenna gain are achieved, compared to the isotropic IBC. In [24] an anisotropic impedance hologram synthesis method is presented, which generates a desired aperture field shaped by space dependent modulation indices and a desired phase distribution. Furthermore, some examples for modulated metasurface antenna designs at low frequencies, e.g., for pencil beam antennas within the X- and the Ka-band and isoflux pattern antennas in the Ka-Band are demonstrated in [24]. A modulated metasurface antenna design with an operation frequency at 300 GHz has been verified by simulations in [25], whose unit cells (UC) are implemented as metallized cylinders.

In [11] the first holographic antenna using the anisotropic IBC is realized on glass technology and verified by far field measurements. The holographic glass antenna provides a pencil beam at 150 GHz and is designed for a hermetically sealed glass package in mm-wave sensor applications. This hologram synthesis is expanded to realize an anisotropic holographic antenna on glass technology generating a conical beam pattern at 77 GHz [1]. The glass antenna is intended for frequency-scanning mm-wave sensor applications and operates within a bandwidth of 20 GHz.

In [26] a modulated impedance surface is designed by using an anisotropic IBC in order to generate multiple beams by using either only a single or multiple feeds. On this foundation, many papers have been published about holographic antennas having multiple feeds [4], [26], [27], [28]. In [29] a holographic multi-feed antenna is designed for an exemplary integration into a monopulse radar.

In recently published works, the hologram superposition into a shared holographic aperture is implemented by a pixel-based arithmetic averaging of all individual impedance sub-holograms [4], [26], [27], [28], [29]. In this design methodology, the incident angular-dependency of the SW w.r.t. the UC is not taken into account and thus, the averaging of the sub-holograms physically corresponds to an arithmetic averaging of the individual pixel geometries. This leads to an increased deviation between the shared holographic aperture and the individual sub-holograms.

In this paper, a novel hologram synthesis method for holographic multi-feed antennas is presented, by taking the UC-related incident angle into account. Furthermore, an eigenvector-based approach to determine the pixel orientation is introduced, for the realization of the impedance tensors by a discrete set of sub-wavelength UCs. In order to optimize the radiation pattern of each feed, a genetic algorithm (GA) is implemented using a 3D-radiation pattern mask as a fitness function. The GA leads to the optimal antenna configuration with the radiation patterns of the shared holographic aperture providing the lowest deviation compared to the ones of the ideal sub-antennas. The holographic multi-feed antenna has four feeds and is intended for the integration into a 2D-monopulse radar system. The antenna prototype is realized on fused silica wafer due to its lower losses at mm-wave frequencies compared to Teflon-based materials and glass enables a very high manufacturing accuracy concerning the wet etching process. The holographic multi-feed antenna is mounted on a multi-layer feeding network. This enables a phase synchronous signal excitation of each feed through rectangular waveguides. The simulation results are verified by measurements of the far field patterns and the S-parameters of the manufactured holographic multi-feed antenna.

This paper is organized as follows: In Section II the novel eigenvector synthesis approach is described. Furthermore, the incident angular-dependent multi-feed hologram synthesis method is introduced. In Section III a comprehensive analytical comparison between the state-of-the-art concept from [4], [26], [27], [28], [29] and the proposed synthesis approach is shown. In Section IV the design of the holographic multi-feed antenna which is intended for the integration into an exemplary 2D-monopulse radar is presented. Section V comprises the realization of the holographic multi-feed antenna prototype on fused silica. The antenna performance is verified by measurements. Finally, the conclusion is drawn in Section VI.

II. SYNTHESIS METHOD FOR MULTI-FEED HOLOGRAMS

A holographic antenna can be realized by a dense periodic structure of sub-wavelength discontinuities ($\approx \frac{\lambda_0}{10}$) placed on a grounded dielectric slab. This structure can be physically seen as a modulated impedance surface representing the impedance hologram. A SW is stimulated by a feed and interacts with the impedance hologram leading to a LW radiation. For this purpose, a SWL excites the fundamental TM_0 SW mode propagating rotationally symmetric on the antenna aperture [11]. Its transverse magnetic field distribution $\underline{\vec{H}}_t$ follows the Hankel function of the second kind and first order [24]. The hologram consists of surface impedance tensors $\underline{\overleftrightarrow{Z}}$ that link the transverse magnetic field $\underline{\vec{H}}_t$ to the transverse electric field distribution $\underline{\vec{E}}_t$ through the space-dependent impenetrable impedance boundary condition (IIBC) as [22]

$$\begin{pmatrix} \underline{E}_{t,x} \\ \underline{E}_{t,y} \end{pmatrix} = \begin{pmatrix} \underline{Z}_{xx} & \underline{Z}_{xy} \\ \underline{Z}_{yx} & \underline{Z}_{yy} \end{pmatrix} \cdot \left(\vec{e}_z \times \begin{pmatrix} \underline{H}_{t,x} \\ \underline{H}_{t,y} \end{pmatrix} \right), \tag{1}$$

where the unit vector $\vec{e}_z$ is aligned normally to the antenna aperture. The isotropic components $\underline{Z}_{xx}$ and $\underline{Z}_{yy}$ are arranged on the main diagonal of the impedance tensor, while on the secondary diagonal the anisotropic ones $\underline{Z}_{xy}$ and $\underline{Z}_{yx}$ are. The IIBC from (1) mathematically represents the interaction of the SW and the impedance hologram. If $\underline{Z}_{xy}$ or $\underline{Z}_{yx}$ exist, a TM/TE SW coupling takes place, and the fundamental TM_0 SW mode is converted into a TM-TE-hybrid LW mode. The transverse electric field distribution resulting from (1) comprises all reactive field contributions, and its spectrum

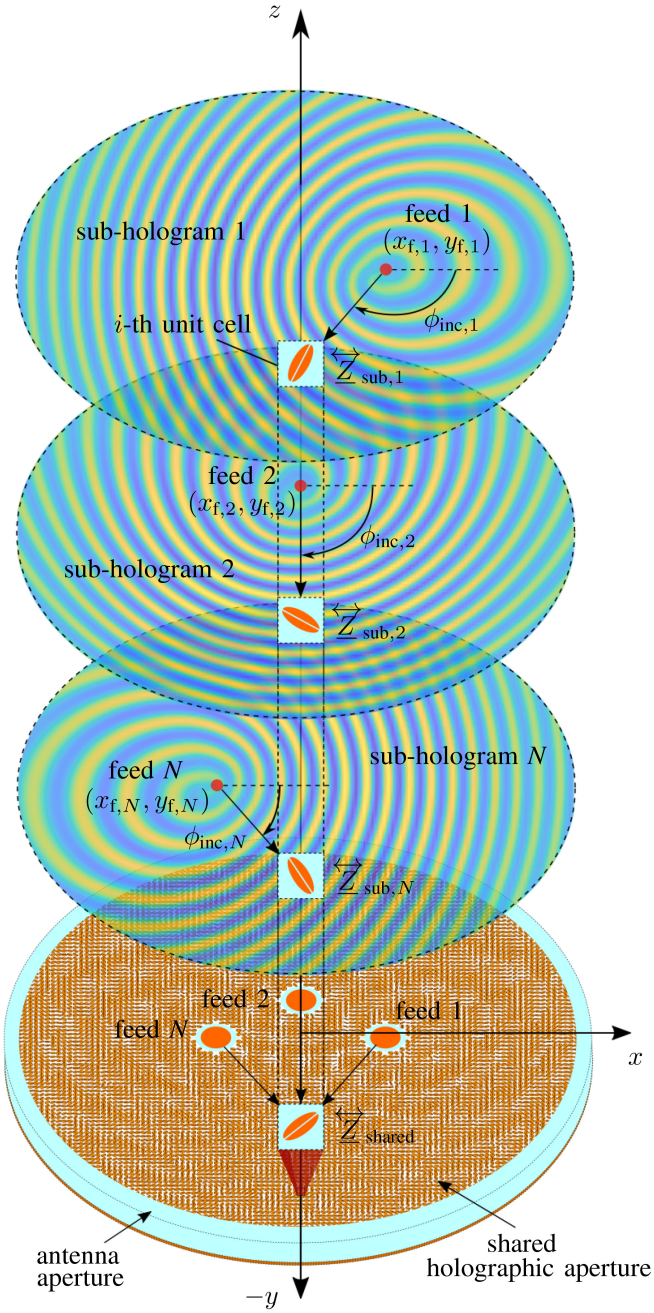

FIGURE 1. Generation of a single physical shared holographic aperture across all N sub-holograms considering the i-th UC-referred incident angle of the respective feed.

is mainly outside the visible region. The objective aperture field distribution $\underline{\vec{E}}_{obj}$ possesses the following form

$$\underline{\vec{E}}_{obj}(x,y) = \vec{T}(x,y) \circ \vec{E}_0 \circ \begin{pmatrix} e^{-j(k_x x)} \\ e^{-j(k_y y \mp \frac{\pi}{2})} \end{pmatrix}, \tag{2}$$

with $\circ$ being the Hadamard product and $\vec{T}(x,y)$ contains the x- and y-components of the desired planar amplitude taper function. The complex phase term may provide an arbitrary polarization, but in this work a circularly polarized excited electric field is used. The constant space independent field amplitudes are described by $\vec{E}_0$. The objective field from (2) corresponds to the electric field distribution of the radiating $(-1,-1)$ LW mode whose spectrum is completely concentrated inside the visible region [30], [31]. The result of the synthesis is an impedance tensor hologram depending on the predefined objective field distribution from (2) and the transverse magnetic field of the SW. The interaction between TM_0 SW mode and the impedance hologram is derived by the IIBC (1) and leads to the radiating portion of the transverse electric field $\underline{\vec{E}}_{t,(-1,-1)}$.

In order to design a holographic antenna having N multiple feeding points, the proposed hologram synthesis method is performed for each feed n located on the antenna aperture at $(x_{f,n},\ y_{f,n})$ (see Fig. 1). Hence, there is a predefined objective aperture field (2) for each feeding point. This leads to N impedance tensor sub-holograms, whose origin corresponds to their feed position. In order to maximize the aperture efficiency, all sub-holograms extend over the whole antenna aperture as depicted in Fig. 1 and reads

$$\mathscr{H}_{sub,n}(x_{f,n},\ y_{f,n}) \quad \forall\, n \in \mathbb{N}. \tag{3}$$

The individual sub-holograms are discretized into I periodically arranged squared UCs, where each i-th UC of a sub-hologram is described by an impedance tensor

$$\underline{\underline{Z}}_{sub,n}(x_{uc,i}, y_{uc,i}) \quad \forall\, n \wedge i \in \mathbb{N}, \tag{4}$$

as shown in Fig. 1. For the implementation of a impedance tensor hologram (3), a complex eigenvalue problem has to be solved depending on the UC-referred incident angle ϕ_{inc} and the pixel geometry [21]. This results in an angular-dependent scalar surface impedance $\underline{Z}_{s,n}(\phi_{inc,n})$. For a meaningful assignment of the tensor to a pixel geometry, the calculation of its corresponding scalar surface impedance, by taking the UC-referred incident angle into account, is necessary (as shown in Fig. 1) [1]. The impedance tensor $\underline{\underline{Z}}_{sub,n}$ from each sub-hologram can be represented by a pixel geometry within a UC. However, only a single impedance hologram realization on the antenna aperture is possible. Therefore, a shared holographic aperture $\mathscr{H}_{shared}$ with an impedance tensor $\underline{\underline{Z}}_{shared}(x_{uc,n},\ y_{uc,n})$ for every UC is created across all N sub-holograms as shown in Fig. 1.

The further course of this section is structured as follows. In Section II-A the general design aspects of holographic multi-feed antennas are discussed. Section II-B briefly deals with the state-of-the-art approach for comparison purposes. In Section II-C, a novel angular-dependent synthesis method is discussed in order to efficiently create the shared holographic aperture. A scalar and a vector-based approach for the anisotropic impedance tensor realization are presented in Sections II-D and II-E, respectively. The simulation results of the three different approaches are evaluated in Section III.

A. GENERAL DESIGN CONSIDERATIONS

The feed positions $(x_{f,n},\ y_{f,n})$ on the antenna aperture (c.f. Fig. 1), from which the cylindrical TM_0 SW typically propagates rotationally symmetric, is subject to the following constrains:

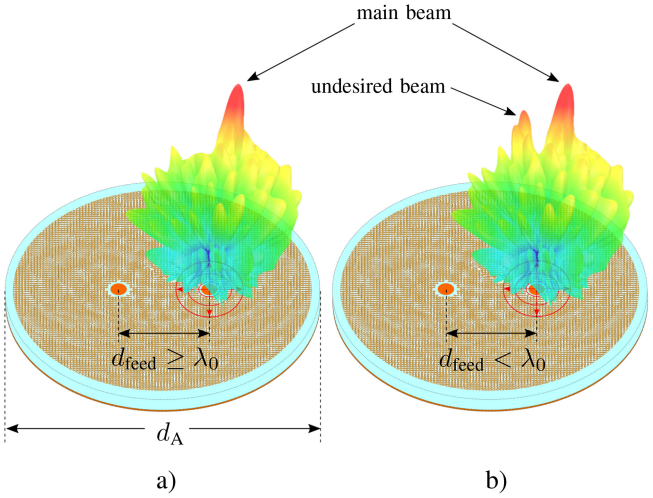

FIGURE 2. Illustration of the effect resulting from the coupling between the feeds on the shared holographic aperture on the radiation pattern of a considered feed. (a) Desired main beam (b) Additional undesired beam.

- The feeds must have a minimum radial distance d_{feed} of λ_0 to one another in order to avoid coupling between their sub-holograms on the shared holographic aperture, which is only a guideline value determined empirically by simulations. If the distance becomes smaller, the SW not only interacts with the primarily excited sub-hologram of the considered feed but is also influenced by the other sub-holograms from the other feeds. This means that in addition to the primary main lobe of the excited feed, the main lobes of the unstimulated feeds are also unintentionally visible in the radiation pattern as exemplary illustrated in Fig. 2.
- Furthermore, the physical dimension of the SWL structure has an influence on the realizable feed position regarding the SWL patch diameter d_{patch} [11]. This means that the minimum realizable radial distance between two feeds corresponds to the patch diameter. Due to the coupling already discussed, in this work the minimum distance is set to

$$d_{\text{feed},n} > d_{\text{patch}} \,\big|\, d_{\text{patch}} \geq \lambda_0. \tag{5}$$

- The maximum antenna aperture size d_{A} (see Fig. 2) also limits the position of the feeds and thus, the aperture efficiency. Therefore, the feeds should be within $0.75\, d_{\text{A}}$.

As a further degree of freedom in the holographic antenna design, the hologram offset ψ_n of the sub-holograms $\mathscr{H}_{\text{sub},n}(\psi_n)$ is introduced. The taper function $\vec{T}_n$ from (2) specifies the amplitude decay in the x-y-plane of the objective aperture field. The transverse modulation period of the sub-hologram results from the interference between the phase distribution of the SW current $\varphi_{\text{SW},n}$ and the objective aperture field $\varphi_{\text{obj},n}$

$$\varphi_n = \varphi_{\text{SW},n} + \varphi_{\text{obj},n}. \tag{6}$$

The hologram offset ψ_n is not subject to any restrictions and can be set arbitrarily. This enables an unrestricted shift of the impedance at the origin of each n-th sub-hologram independently of the feed position. The impedance hologram phase expression is defined as

$$\varphi_n = \varphi_{\text{SW},n} + \varphi_{\text{obj},n} + \psi_n. \tag{7}$$

B. ANGULAR-INDEPENDENT SYNTHESIS METHOD

For the sake of comparison, the current state-of-the-art approach for holographic multi-feed antenna designs is briefly introduced. The hologram superposition is implemented by a pixel-wise angular-independent arithmetic averaging (AiA) of all N sub-holograms to a shared holographic aperture (c.f. Fig. 1) [4], [26], [27], [28], [29] as

$$\mathscr{H}_{\text{shared}} = \frac{1}{N}\sum_{n=1}^{N} \mathscr{H}_{\text{sub},n}. \tag{8}$$

Each sub-hologram consists of a discrete set of UCs which physically represent the impedance tensor $\overleftrightarrow{\underline{Z}}_{\text{sub},n}$ (see Fig. 1). This arithmetic averaging approach of all sub-holograms is performed for each i-th UC

$$\overleftrightarrow{\underline{Z}}_{\text{shared}}(i) = \frac{1}{N}\sum_{n=1}^{N} \overleftrightarrow{\underline{Z}}_{\text{sub},n}(i). \tag{9}$$

This design methodology features of simple pixel combination, but it does not take the angular-dependency of the UCs surface impedance into account. The deviation of the shared holographic aperture $\mathscr{H}_{\text{shared}}$ to each n-th individual sub-hologram $\mathscr{H}_{\text{sub},n}$ leads to an absolute hologram error $\mathscr{H}_{\text{error}}$

$$\mathscr{H}_{\text{error}} = \sum_{n=1}^{N} \left| \mathscr{H}_{\text{sub},n} - \mathscr{H}_{\text{shared}} \right|. \tag{10}$$

Since each sub-hologram is realized by a discrete set of UCs, representing the impedance tensor $\overleftrightarrow{\underline{Z}}_{\text{sub},n}$, the arithmetic averaging of all sub-holograms results in an impedance error for each UC on the shared antenna aperture [30]:

$$\overleftrightarrow{e}(i) = \sum_{n=1}^{N} \left| \overleftrightarrow{\underline{Z}}_{\text{sub},n}(i) - \overleftrightarrow{\underline{Z}}_{\text{shared}}(i) \right|. \tag{11}$$

The impedance error directly influences the synthesized objective aperture field distribution of the shared holographic aperture $\mathscr{H}_{\text{shared}}$. Thus, an increased deviation of the synthesized radiation patterns from the ideal radiation patterns, which originate from the ideal sub-holograms $\mathscr{H}_{\text{sub},n}$, can be observed.

C. ANGULAR-DEPENDENT SYNTHESIS METHOD

To overcome the drawbacks of the state-of-the-art approach (Section II-B), a novel angular-dependent synthesis method for holographic multi-feed antennas is presented and discussed throughout the following points (see Fig. 3).

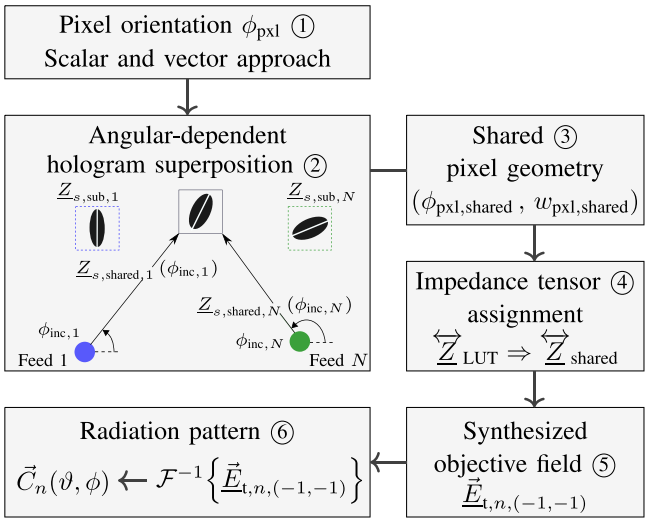

FIGURE 3. Analytical angular-dependent synthesis method for holographic multi-feed antennas [30].

- *Angular-Dependent Hologram Superposition ②:* In this synthesis approach, the N sub-holograms are not averaged. Instead, a shared holographic aperture depending on the UC-referred incident angle $\phi_{\mathrm{inc},n}$ is determined as depicted in ② in Fig. 3. The pixel geometry to realize the surface impedances $\underline{Z}_{s,\mathrm{sub},n}$ of every UC is depicted in Fig. 4. To improve the anisotropic degree, an slot-loaded elliptical pixel shape is realized. Thus, the SW current tends to flow along the slot and additionally along the direction of the ellipse resulting in an increased electric field portion in the TE component and an enhanced anisotropic degree. The pixel is defined by its corresponding orientation angle ϕ_{pxl} and the pixel width w_{pxl}. The length of the elliptical shape l_{pxl} remains unchanged (see Fig. 4). The angular-dependent hologram superposition is based on a two-step procedure. First, the orientation of the shared pixel $\phi_{\mathrm{pxl,shared}}$ which has a minimum error to the ideal sub-pixel orientations $\phi_{\mathrm{pxl},n}$ is computed for every UC. Second, the UC-referred incident angle $\phi_{\mathrm{inc},n}$ of each feed is added to the orientation of the shared pixel (see ② in Fig. 3). This leads to a look-up table (LUT) $\underline{Z}_{s,\mathrm{LUT}}$ having N rows defined by the angular-dependent pixel orientations and M columns for the different pixel widths, containing all corresponding scalar impedance values

$$\underline{Z}_{s,\mathrm{LUT}}\left(\phi_{\mathrm{pxl,shared}} + \phi_{\mathrm{inc},n},\, w_{\mathrm{pxl},m}\right) \quad \forall\, m \in \mathbb{N}. \tag{12}$$

It is worth to note that $\underline{Z}_{s,\mathrm{LUT}}$ consists of an impedance line vector for each n-th incident angular-dependent pixel orientation $\phi_{\mathrm{pxl,shared}} + \phi_{\mathrm{inc},n}$ and comprises all scalar impedance values as a function of the pixel widths. The goal is to find the minimum impedance error across all the individual sub-impedances compared to the LUT impedance column vectors to determine the shared pixel width $w_{\mathrm{pxl,shared}}$ for each UC. Forming the row sum over all columns results in a scalar surface impedance error vector $\vec{e}(w_{\mathrm{pxl},m})$ for every pixel width

$$\vec{e}\left(w_{\mathrm{pxl},m}\right) = \sum_{n=1}^{N} \left| \underline{Z}_{s,\mathrm{LUT}}\left(\phi_{\mathrm{pxl,shared}} + \phi_{\mathrm{inc},n},\, w_{\mathrm{pxl},m}\right) - \underline{Z}_{s,\mathrm{sub},n} \right|. \tag{13}$$

Afterwards, the shared pixel width is determined by the column with the lowest impedance error value

$$w_{\mathrm{pxl,shared}} = \underset{w_{\mathrm{pxl},m}}{\operatorname{argmin}} \left\{ \vec{e}\left(w_{\mathrm{pxl},m}\right) \right\}. \tag{14}$$

- *Shared Pixel Geometry ③:* This leads to the shared pixel geometry $(\phi_{\mathrm{pxl,shared}}\ w_{\mathrm{pxl,shared}})$ with a minimum error regarding the N sub-geometry values for every UC. All shared pixel geometries constitute the shared holographic aperture $\mathscr{H}_{\mathrm{shared}}$ (see ③ in Fig. 3).
- *Impedance Tensor Assignment ④:* The shared impedance tensor $\overleftrightarrow{\underline{Z}}_{\mathrm{shared}}$ is determined by the 3D-tensor LUT $\overleftrightarrow{\underline{Z}}_{\mathrm{LUT}}$ by using the shared pixel geometry (see ④ in Fig. 3).

$$\overleftrightarrow{\underline{Z}}_{\mathrm{shared}} = \overleftrightarrow{\underline{Z}}_{\mathrm{LUT}}\left(\phi_{\mathrm{pxl,shared}},\, w_{\mathrm{pxl,shared}}\right). \tag{15}$$

The LUT has $N \times M \times 4$ entries for the angular-dependent pixel orientations, the pixel widths and for the 4 tensor components.

- *Synthesized Objective Aperture Field and Radiation Pattern ⑤–⑥:* Finally, the objective aperture field distribution is calculated using the IIBC (1). This leads to the electric field of the radiating $(-1,-1)$ LW mode and its corresponding far field pattern $\vec{C}_n$ for each feed (see ⑤ and ⑥ in Fig. 3).

To perform the angular-dependent hologram superposition (② in Fig. 3), the prior knowledge about the pixel orientation $\phi_{\mathrm{pxl},n}$ for every UC of each individual sub-hologram must be calculated in advance. The pixel orientation is necessary to realize the anisotropic effect of the tensor. Hence, a scalar and a vector approach are presented in Sections II-D and II-E that ensure an unambiguous assignment between the angular-dependent analytical scalar impedance and the pixel orientation (see ① in Fig. 3).

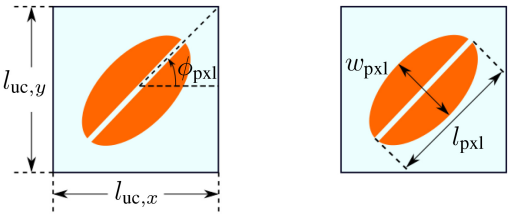

FIGURE 4. Elliptical 2π-periodic pixel structure with an additional slot through the center within the unit cell.

D. PIXEL ORIENTATION - SCALAR APPROACH

The amplitudes of $\underline{Z}_{xy,n}$ and $\underline{Z}_{yx,n}$ do not allow for an assignment of the anisotropic degree to an unambiguous pixel

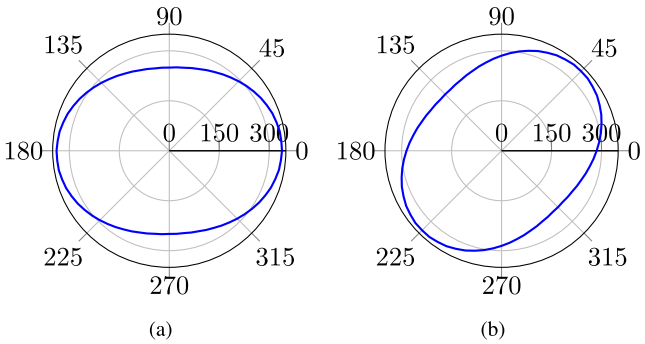

FIGURE 5. Angular-dependent scalar impedance of a slot-loaded elliptical pixel vs. the UC-referred incident angle range $\phi_{\text{inc}} = [0°, 360°]$ at the fixed slot angle (a) $\phi_{\text{pxl}} = 0°$ and (b) $\phi_{\text{pxl}} = 45°$ at 77 GHz. (a) $\theta_{\text{pxl}} = 0°$. (b) $\theta_{\text{pxl}} = 45°$.

orientation within a 2π-period, since the amplitude curve has two intersections with the same value. Only the phase distribution of the anisotropic tensor components φ_{xy} or φ_{yx} offers an unambiguous assignment of the pixel orientation and the anisotropic degree [30]

$$\varphi_{xy}(x, y) = \beta_{\text{SW}}\sqrt{x^2 + y^2} - \left(k_x x + k_y y\right) + \phi_{\text{inc}}, \quad (16)$$

where $\varphi_{xy} = \varphi_{yx}$, β_{SW} is the SW phase constant, and k_x, k_y are the wavenumbers along the x- and y-direction, respectively. As a result, every UC of each n-th sub-hologram has a pixel orientation $\phi_{\text{pxl},n}$ due to its anisotropic tensor components. The orientation of the shared pixel $\phi_{\text{pxl,shared}}$ is computed under the condition of the minimum error to all the individual slot angles $\phi_{\text{pxl},n}$ for each UC for the following two cases:

- $\max\{\phi_{\text{pxl},n} + \phi_{\text{inc},n}\} - \min\{\phi_{\text{pxl},n} + \phi_{\text{inc},n}\} \leq 90°$:

$$\phi_{\text{pxl,shared}} = \frac{1}{N}\sum_{n=1}^{N} \phi_{\text{pxl},n} + \phi_{\text{inc},n}. \quad (17)$$

- $\max\{\phi_{\text{pxl},n} + \phi_{\text{inc},n}\} - \min\{\phi_{\text{pxl},n} + \phi_{\text{inc},n}\} > 90°$:

$$\phi_{\text{pxl,shared}} = \left(\frac{1}{N}\sum_{n=1}^{N} \phi_{\text{pxl},n} + \phi_{\text{inc},n}\right) + 90°. \quad (18)$$

The expression max and min denote the maximum and the minimum angular-dependent orientation of the sub-pixels across all sub-holograms. Subsequently, the shared pixel width, which yields the lowest impedance error, is calculated by the incident angle-dependent hologram superposition algorithm (see ③ in Fig. 3) [30]. The shared geometry parameters determine the impedance tensor as function of the incident angle $\phi_{\text{inc},n}$ (see ④ in Fig. 3). This results in an unambiguous pixel geometry for the scalar impedance and the corresponding impedance tensor.

E. PIXEL ORIENTATION - EIGENVECTOR APPROACH

In the scalar approach, only the anisotropic tensor components $\underline{Z}_{xy,n}$ and $\underline{Z}_{yx,n}$ are considered to assign the pixel orientation. The pixel width is primarily determined by the isotropic components $\underline{Z}_{xx,n}$ and $\underline{Z}_{yy,n}$, while the orientation angle of the pixel is mainly defined by the anisotropic tensor

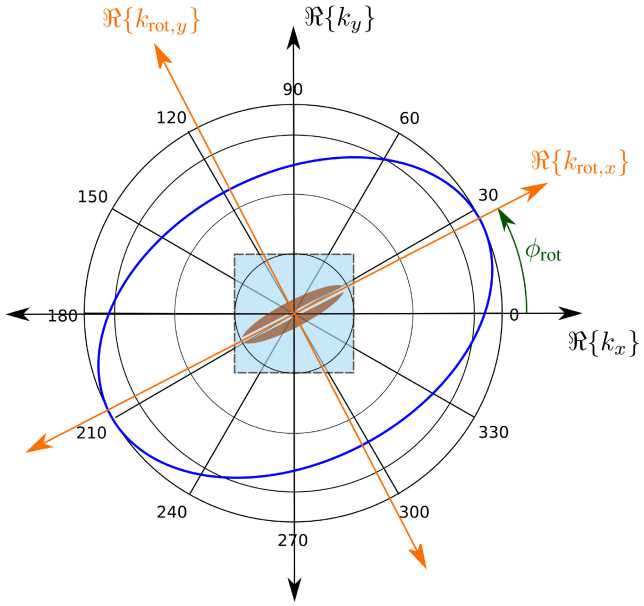

FIGURE 6. Coordinate system rotation in the k_x-k_y-plane for pixel orientation extraction.

components on its secondary diagonal. Since the SW current tends to flow along the slot and additionally along the direction of the elliptical shape, the pixel width also has an influence on the anisotropic degree of the pixel. Therefore, the isotropic and anisotropic tensor components must be considered for the assignment of the pixel orientation in order to realize the impedance tensor more accurately. The scalar impedance vs. the incident angle has a peanut-shaped course for an anisotropic pixel geometry as depicted in Fig. 5. In Fig. 5(a) the maximum and minimum are located on the principal axes and thus the pixel orientation ϕ_{pxl} can be determined to $\phi_{\text{pxl}} = 0°$. Since $\phi_{\text{inc}} = \phi_{\text{pxl}}$ applies, no TM/TE SW coupling occurs and thus, no anisotropic behaviour is present. Hence, the secondary diagonal is zero $\underline{Z}_{xy,n} = \underline{Z}_{yx,n} = 0\ \Omega$ and the tensor corresponds to a diagonal tensor. For an anisotropic behaviour of the pixel geometry, a rotation of the principal axis around the rotation angle ϕ_{rot} takes place, as illustrated in Fig. 5(b), and the tensor is no longer a diagonal matrix, since its secondary diagonal corresponds to $\underline{Z}_{xy,n} \neq 0\ \Omega$ and $\underline{Z}_{yx,n} \neq 0\ \Omega$. A diagonalisation of the impedance tensor $\overleftrightarrow{\underline{Z}}$ is used in order to directly determine the pixel orientation angle for every anisotropic impedance tensor. The diagonalisation process corresponds to a rotation of the principal axes of the coordinate system around ϕ_{rot} in the $\Re\{k_x\}$-$\Re\{k_y\}$-plane, as depicted in Fig. 6, where the rotation tensor $\overleftrightarrow{R}$ is defined by

$$\overleftrightarrow{R}(\phi_{\text{rot}}) = \begin{pmatrix} \cos(\phi_{\text{rot}}) & \sin(\phi_{\text{rot}}) \\ -\sin(\phi_{\text{rot}}) & \cos(\phi_{\text{rot}}) \end{pmatrix}. \quad (19)$$

The impedance tensor is diagonalised by

$$\overleftrightarrow{\underline{T}}(\phi_{\text{rot}}) = \overleftrightarrow{R}^{-1}(\phi_{\text{rot}}) \cdot \overleftrightarrow{\underline{Z}} \cdot \overleftrightarrow{R}(\phi_{\text{rot}}). \quad (20)$$

The rotation angle at which the secondary diagonal $\underline{T}_{xy}$ and $\underline{T}_{yx}$ vanish has to be found resulting in the diagonal tensor

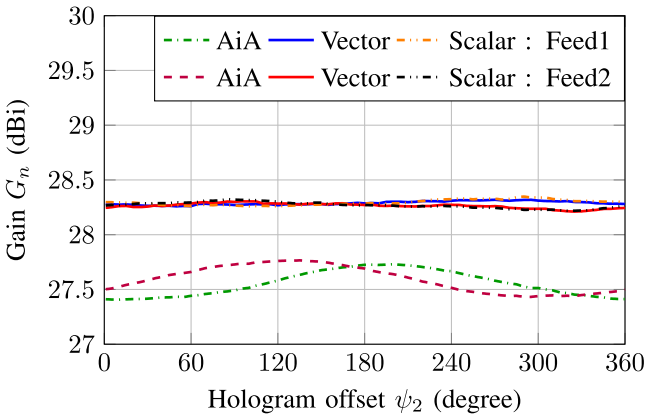

FIGURE 7. Analytical antenna gain vs. the impedance hologram offset of feed 2 $\psi_2 = [0°, 360°]$ where the feeds are located at ($x_{f,1,2} = \pm 3$ mm, $y_{f,1,2} = 0$ mm) for 77 GHz.

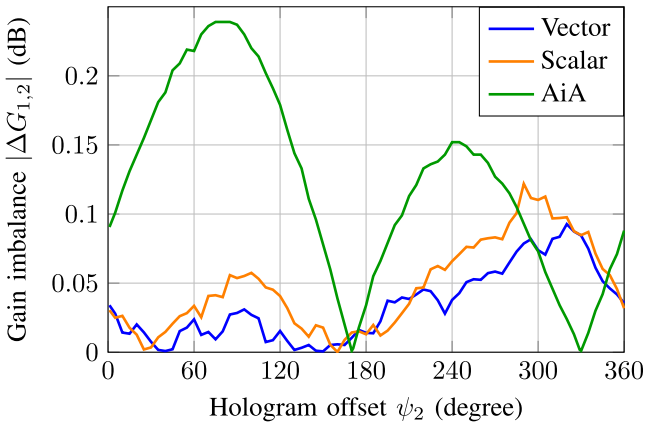

FIGURE 8. Gain imbalance vs. the impedance hologram offset of feed 2 $\psi_2 = [0°, 360°]$ where the feeds are located at ($x_{f,1,2} = \pm 3$ mm, $y_{f,1,2} = 0$ mm) for 77 GHz.

$\underleftrightarrow{T}$ and the required rotation angle ϕ_{rot}

$$\phi_{\text{rot}} \Leftarrow \underleftrightarrow{R}^{-1} \cdot \underleftrightarrow{Z} \cdot \underleftrightarrow{R}(\phi_{\text{rot}})\big|_{\underline{T}_{xy}=\underline{T}_{yx}=0\ \Omega} . \tag{21}$$

The result is an impedance tensor $\underleftrightarrow{T}$ with no TM/TE SW coupling, since the principal axes are rotated by ϕ_{rot} in such a way that they are located in the maximum and minimum at $\Re\{k_{\text{rot},x}\}$ and $\Re\{k_{\text{rot},y}\}$ as depicted in Fig. 6.

This results in an unambiguous pixel orientation angle $\phi_{\text{pxl},n}$ using all impedance tensor components for every UC of all sub-holograms. The orientation of the shared pixel $\phi_{\text{pxl,shared}}$ is calculated by (17) and (18) in such a way that it has the lowest pixel angle error compared to all the individual pixel angles $\phi_{\text{pxl},n}$. Afterwards, the incident angular-dependent synthesis method from Section II-C is used to determine the shared pixel width $w_{\text{pxl,shared}}$ having the lowest impedance error to all ideal analytical impedance sub-holograms.

III. ANALYTICAL COMPARISON

In order to compare the angular-independent method (Section II-B) and the two angular-dependent approaches (Section II-C), a holographic multi-feed antenna is designed having two feeds at ($x_{\text{f},1} = 3$ mm, $y_{\text{f},1} = 0$ mm) and ($x_{\text{f},2} = -3$ mm, $y_{\text{f},2} = 0$ mm) at an operation frequency of 77 GHz. The hologram offset of feed 1 remains $\psi_1 = 0°$ while $\psi_2 = [0°, 360°]$ varied in order to investigate its influence on the antenna gain, side-lobe level, polarization purity, and gain imbalance of the holographic multi-feed antenna. The holographic antenna is intended to radiate a right-handed circular polarized (RHCP) single beam for each feed in azimuth direction $\phi_{0,1/2} = 0°$ and is tilted to an elevation angle of $\vartheta_{0,1} = 5°$ and $\vartheta_{0,2} = -5°$, respectively. The antenna consists of 14 400 squared UCs, and to ensure a homogeneous periodic structure, the UC size is set to 0.4 mm × 0.4 mm, which results in an aperture size of 48 mm × 48 mm.

In Fig. 7 the analytically calculated antenna gain vs. the hologram offset range between 0° and 360° is shown. The antenna based on the AiA approach has a maximum analytical gain of 27.7 dBi, where losses and the reflection coefficient are not taken into account. For both the scalar and vector approach the same gain of 28.3 dBi is achieved, which is increased by 0.6 dB compared to the AiA method. This means that with the scalar or vector approach 15 % less aperture area is necessary to achieve the same antenna gain as with the AiA approach. The antenna gain differs negligibly from the scalar to the vector pixel orientation approach, since the same angle-dependent synthesis algorithm was used. The gain almost remains constant over the whole hologram offset range, whereas for the AiA synthesis method a maximum peak-to-peak deviation of 0.4 dB can be determined (see Fig. 7). The maximum gain imbalance $|\Delta G_{\max}|$ describes the maximum deviation of the antenna gain between all N feeds and equals the triangular matrix

$$|\Delta G_{\max}| = \max \begin{pmatrix} \Delta G_{1,2} & \dots & \dots & \Delta G_{1,N} \\ 0 & \ddots & \ddots & \vdots \\ \vdots & \ddots & \ddots & \vdots \\ 0 & \dots & 0 & \Delta G_{N-1,N} \end{pmatrix} . \tag{22}$$

As the impedance value in the origin of the sub-hologram changes across the hologram offset, the sub-holograms of the AiA approach are almost mirror symmetric at 172°, and the gain imbalance becomes zero. The increased impedance error of the angular-independent approach (Section II-B) leads to a maximum gain imbalance of 0.24 dB (Fig. 8). For a hologram offset of 85° and 245° two local maxima of the gain imbalance exist, since the individual impedance tensor entries for each UC of both sub-holograms are orthogonal to one another. This leads to the two maxima of the gain imbalance within 360° of the hologram offset. The angular-dependent scalar and the vector approach have two local maxima and two local minima, almost for the same hologram offset values. This again results from the fact that the same incident angle-dependent algorithm was used for the multi-feed synthesis. However, the maximum imbalance with the vector approach is only 0.08 dB and therefore 0.04 dB lower

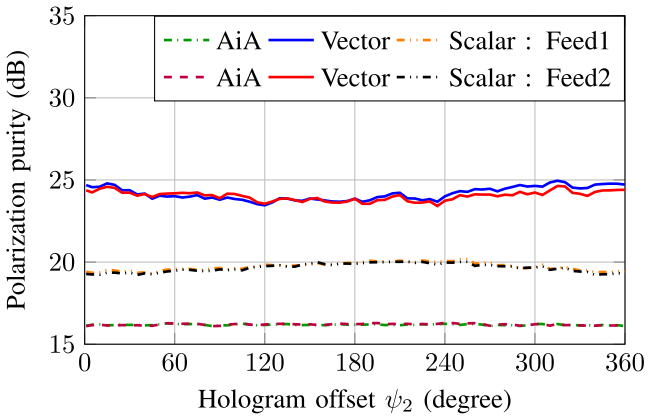

FIGURE 9. Polarization purity vs. the impedance hologram offset of feed 2 $\psi_2 = [0°, 360°]$ where the feeds are located at ($x_{f,1,2} = \pm 3$ mm, $y_{f,1,2} = 0$ mm) for 77 GHz.

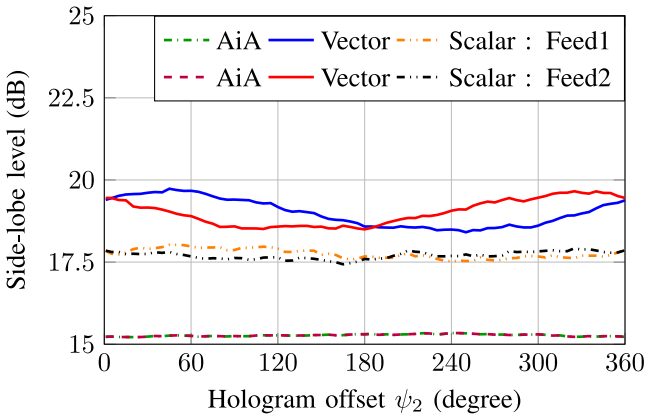

FIGURE 10. Side-lobe level vs. the impedance hologram offset of feed 2 $\psi_2 = [0°, 360°]$ where the feeds are located at ($x_{f,1,2} = \pm 3$ mm, $y_{f,1,2} = 0$ mm) for 77 GHz.

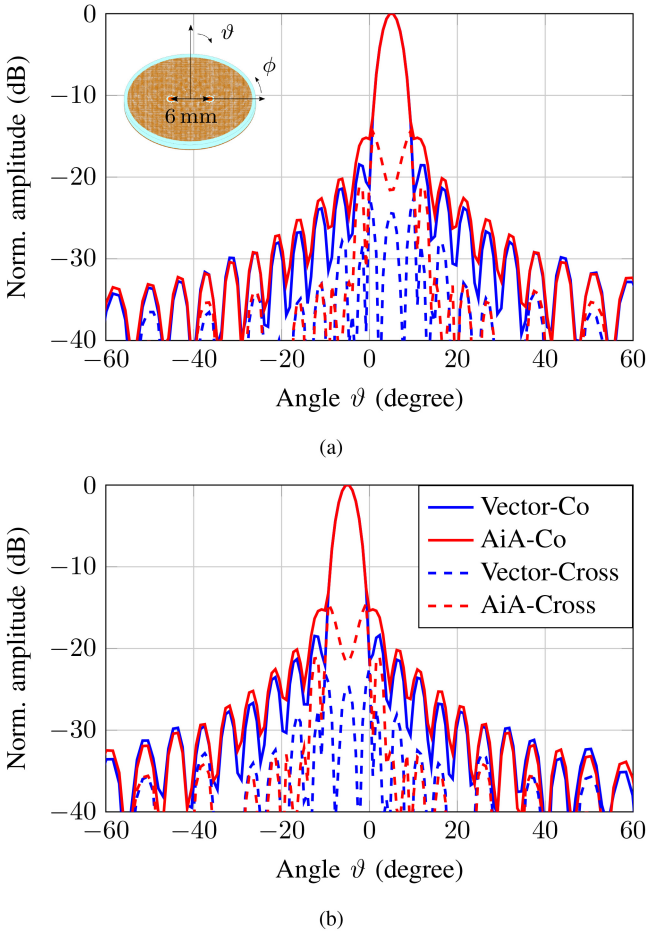

FIGURE 11. Radiation pattern with two feeds at $x_{f,1,2} = \pm 3$ mm, $y_{f,1,2} = 0$ mm with the proposed pixel mapping algorithm with the hologram offsets $\psi_1 = 0°$ and $\psi_2 = 150°$ and the AiA approach with an impedance hologram offset of $\psi_1 = 0°$ and $\psi_2 = 172°$ at 77 GHz. (a) feed 1 at $\phi_0 = 0°$ (b) feed 2 at $\phi_0 = 0°$.

compared to the scalar approach (Fig. 8). This improvement of the gain imbalance results from the vector-based assignment of the pixel orientation. For a hologram offset of up to 180° the vector approach provides a maximum imbalance of 0.03 dB revealing a very wide design range for ψ_2 with a negligible gain imbalance. The disregard of the angular-dependency leads to an almost flat polarization purity of only 16 dB (Fig. 9) over the hologram offset. The assignment of the pixel orientation is primarily responsible for the polarization purity of the holographic antenna. For the scalar pixel orientation approach, there is an improvement of the polarization purity increasing by 4 dB to 20 dB. However, since the slot-loaded elliptical pixel geometry (see Fig. 4) is used in this work, all tensor components must be considered in the pixel orientation calculation. Therefore, the vector approach from Section II-E results in a further improvement in the polarization purity of up to 25 dB due to the enhancement of the anisotropic pixel orientation as depicted in Fig. 9.

The side-lobe level (SLL) (see Fig. 10) shows an improvement compared to the AiA method by at least 3.25 dB to a total of 18.5 dB as the angular-dependent hologram superposition was used. The angle-dependent vector approach synthesizes the electric object aperture field distribution more accurately and thus improves the SLL.

The simulated radiation patterns for the AiA approach and the angular-dependent vector method are illustrated in Fig. 11 for elevation angles in the range ±60° at the azimuth angle 0°. The hologram offset of the first feed remains $\psi_1 = 0°$ for both approaches and for the second feed $\psi_2 = 172°$ for the AiA method and $\psi_2 = 150°$ for the vector approach. In this way, both the SLL improve by 3.25 dB and an enhancement of polarization purity by 4 dB for the vector approach is achieved in comparison with the AiA method (see Fig. 11). In the next step, the distance between two feeds is varied from 6 mm ($1.5\lambda_0$) to 20 mm ($5\lambda_0$). The polarization purity in Fig. 12 converges towards the same value. If the feeds are positioned very close to each other ($1.5\lambda_0$), the polarization purity increases by 10 dB due to the improved pixel orientation of the vector approach. As the distance between the feeds increases to $5\lambda_0$, the feeds are pushed to the edge of the antenna aperture. Thereby, the spiral shape of the impedance sub-holograms on the shared holographic aperture is lost, and $\vec{E}_{x,n}$ becomes dominant

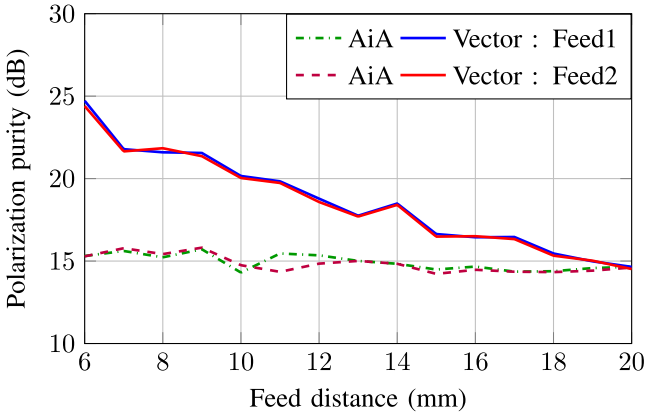

FIGURE 12. Polarization purity vs. the distance between two feeds in the range $[1.5\lambda_0, 5\lambda_0]$ with a hologram offset of $\psi_1 = \psi_2 = 0°$ using the angular-independent AiA approach and the proposed eigenvector-based angular-dependent hologram synthesis method at 77 GHz.

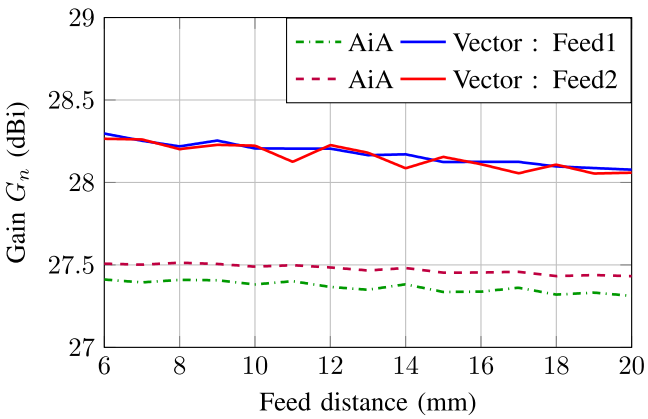

FIGURE 13. Analytical antenna gain vs. the distance between two feeds in the range $[1.5\lambda_0, 5\lambda_0]$ with a hologram offset of $\psi_1 = \psi_2 = 0°$ using the angular-independent AiA approach and the proposed eigenvector-based angular-dependent hologram synthesis method at 77 GHz.

w.r.t. $\underline{\vec{E}}_{y,n}$ or vice versa, which leads to a linearly polarized electromagnetic field radiation. Hence, the radiation of the circularly polarized electromagnetic field of the holographic antenna is reduced. This is why the polarization purity for the AiA method and the angular-dependent vector approach converges towards the same value with increasing feed distance. Furthermore, the gain imbalance $|\Delta G_{1,2}|$ between the two feeds remains constant at 0.12 dB in the AiA approach and a maximum gain imbalance over the hologram offset of 0.05 dB for the vector approach is achieved (see Fig. 13). In Fig. 13 the gain is shown for the AiA method and the vector approach. The gain decreases with a larger distance between the feeds to almost the same extent for both approaches. But the gain is improved by 0.75 dB across the whole hologram offset of 360°. The SLL also deteriorates vs. the feed distance, but the vector approach (Section II-E) remains almost constantly 4 dB better compared to the AiA approach from Section II-B (see Fig. 14).

Moreover, the number of feeds is continuously increased from 2 to 8, and the feeds are arranged equidistantly on a

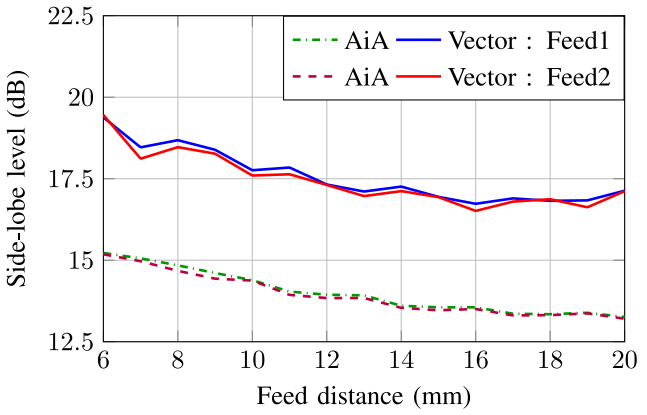

FIGURE 14. Side-lobe level vs. the distance between two feeds in the range $[1.5\lambda_0, 5\lambda_0]$ with a hologram offset of $\psi_1 = \psi_2 = 0°$ using the angular-independent AiA approach and the proposed eigenvector-based angular-dependent hologram synthesis method at 77 GHz.

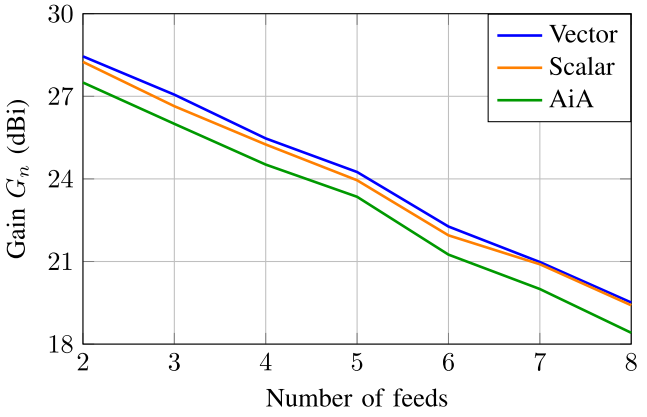

FIGURE 15. Analytical antenna gain vs. the number of feeds from 2 to 8 which are arranged equidistantly on a circle at 77 GHz.

circle with a distance of $1.5\lambda_0$ where the feed positions $x_{\mathrm{f},n}$ and $y_{\mathrm{f},n}$ are defined as

$$x_{\mathrm{f},n} = \frac{1.5\lambda_0 N}{2\pi} \cos\left(\frac{n360°}{N}\right) \tag{23}$$

$$y_{\mathrm{f},n} = \frac{1.5\lambda_0 N}{2\pi} \sin\left(\frac{n360°}{N}\right). \tag{24}$$

The hologram offset is set to $\psi_n = 0°$ for all the N sub-holograms $\mathscr{H}_{\mathrm{sub},n}(\psi_n)$. The analytical antenna gain (see Fig. 15) of the scalar and vector approach is almost identical as the same angular-dependent hologram superposition algorithm was used. Furthermore, a gain improvement of at least 0.7 dB compared to AiA approach vs. the number of feeds is evident. The gain decreases almost identically for all three approaches, because each additional feed leads to an additional sub-hologram. The increasing number of the sub-holograms leads to an increase of the error compared to the shared holographic aperture (10) and thus a rising impedance error results for each UC (11) and the gain decreases.

This leads to an increased discrepancy in the synthesis of the objective aperture field. Hence, the SLL deteriorates as the number of feeds increases as depicted in Fig. 16.

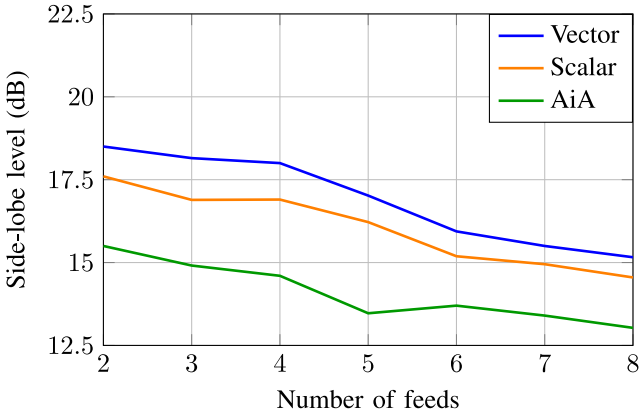

FIGURE 16. Side-lobe level vs. the number of feeds from 2 to 8 which are arranged equidistantly on a circle at 77 GHz.

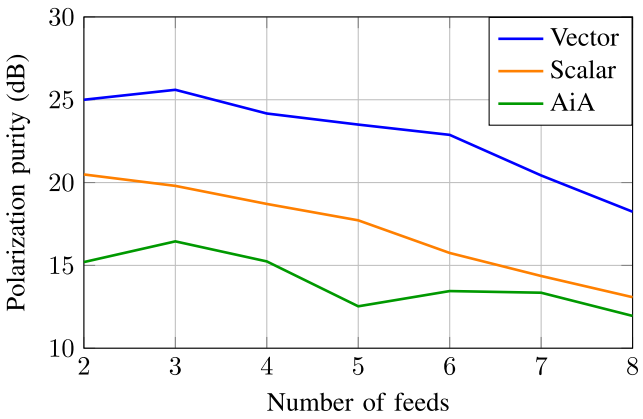

FIGURE 17. Polarization purity vs. the number of feeds from 2 to 8 which are arranged equidistantly on a circle at 77 GHz.

The polarization purity of the vector approach is enhanced by up to 10 dB compared to the AiA approach and is constantly 5 dB higher than the scalar method (see Fig. 17), since the vector approach considers the entire impedance tensor to determine the sub-pixel orientation for each UC.

IV. DESIGN OF THE HOLOGRAPHIC MULTI-FEED ANTENNA

Based on the novel angular-dependent hologram synthesis method discussed in Section II, a holographic multi-feed antenna is designed, according to the flow diagram in Fig. 3. In this work, the holographic multi-feed antenna is intended for an integration into a 2D-monopulse radar system. As a consequence, the antenna provides four feeds which excites a pencil beam characteristic tilted pairwise in the elevation and in the azimuth plane, respectively. The 2D-monopulse radar principle allow a 2D-direction of arrival (DoA) estimation in both azimuth and elevation by comparing the amplitudes of the sum and differential beams [32]. In order to achieve a field of view (FoV) of 10° at 77 GHz the objective aperture fields from (2) were defined to reach a 3-dB-beamwidth of 5°. The steering angles are tilted in the azimuth and elevation plane as listed in Table 1. The lithographic

TABLE 1. Steering angles of the holographic multi-feed antenna for each individual feed at 77 GHz.

Feed number	1	2	3	4
$\vartheta_{0,n}$	3°	−3°	3°	−3°
$\phi_{0,n}$	45°	45°	135°	135°

manufacturing process of the holographic multi-feed antenna allows a maximum antenna aperture size of 48 mm × 48 mm. The antenna consists of 14 400 squared UCs, and the UC size is set to 0.4 mm × 0.4 mm to ensure a homogeneous periodic structure. The thickness of the fused silica wafer is set to 500 µm in order to excite only the fundamental TM_0 SW mode. The pixel geometry is based on an elliptically shaped metal patch with an inclined slot (see Fig. 4) to realize anisotropic impedance tensors. The orientation of the slot-loaded ellipse is determined by the eigenvector approach from Section II-E by using all impedance tensor components in order to increase the polarization purity. The realization of the analytical shared holographic aperture relies on a preliminary constructed impedance LUT which links the analytical impedance tensor to the corresponding pixel geometry. The elliptical pixel has a constant length of $l_{\mathrm{pxl}} = 390\,\mu\mathrm{m}$, while the width w_{pxl} is varied from 39 µm to 390 µm to cover an aspect ratio (AR) range of [0.1, 1]. The inclined slot has a width of 20 µm. An AR lower than 0.1 is physically not processable, as the area of the elliptical patch becomes too small in relation to the slot width.

The UC dimensions and the pixel geometry provide an average impedance of $\underline{Z}_{\mathrm{avg}} = \mathrm{j}322.75\ \Omega$ and a maximum modulation index of $\max\{M_{x,y}\} = 0.13$.

The shared holographic aperture is computed by a non-pixel-based GA. The block diagram of the flow diagram of the GA is depicted in Fig. 18. First, an assortment of L feed positions $(x_{\mathrm{f},n,l}, y_{\mathrm{f},n,l})$ and hologram offsets $\psi_{n,l}$ are randomly selected for each feed to create an initial start population regarding the general design considerations described in Section II-A (see ① in Fig. 18). This population consists of all the L selected individuals of the GA. Subsequently, the ideal sub-holograms $\mathscr{H}_{\mathrm{sub},n,l}$ are calculated by the hologram synthesis method from Section II which belong to the ideal sub-antennas of each feed. The pixel orientation of each sub-hologram is calculated based on the eigenvector approach from Section II-E for every UC. Next, the orientation of the shared pixel for all sub-holograms is calculated with (17) and (18) for each UC. Afterwards, the incident angular-dependent hologram synthesis method from Section II-C is performed resulting in a shared holographic aperture $\mathscr{H}_{\mathrm{shared},l}$ for each individual of the GA. Thus, the shared analytical impedance tensor of each UC on the antenna aperture has a corresponding pixel geometry (see ② in Fig. 18).

The goal of the GA is to find a shared holographic aperture, whose radiation patterns $\vec{C}_{\mathrm{shared},n}$ have the lowest error compared to the radiation patterns of the ideal sub-antennas $\vec{C}_{\mathrm{ideal},n}$. For this purpose, a 3D-radiation pattern mask for the

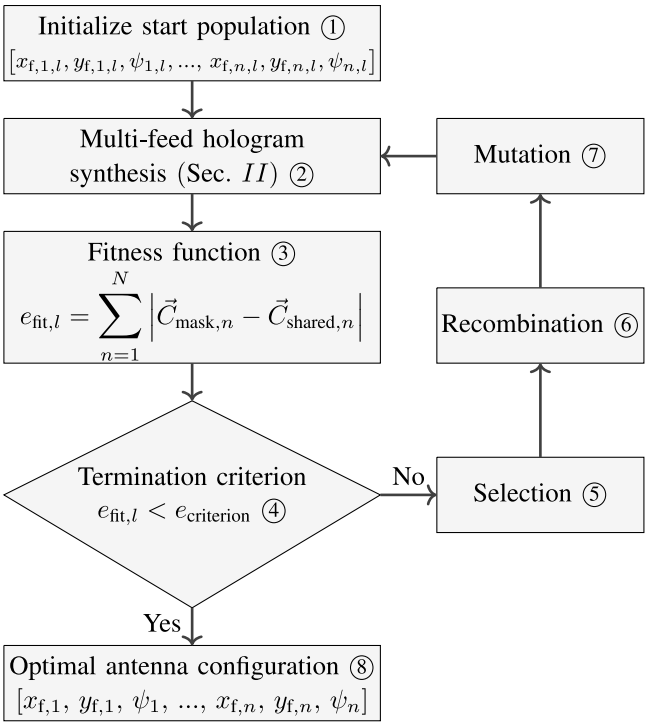

FIGURE 18. Block diagram of the genetic algorithm for holographic multi-feed antennas.

TABLE 2. Optimal antenna configuration concerning feeds and hologram offset resulting from the GA at 77 GHz.

Feed number	1	2	3	4
$x_{f,n}$	−1.4 mm	2.0 mm	−1.6 mm	−2.8 mm
$y_{f,n}$	0.2 mm	10.4 mm	−6.0 mm	8.2 mm
ψ_n	195°	160°	70°	40°

co- and cross-polarization $\vec{C}_{mask,co,n}$, $\vec{C}_{mask,cross,n}$ is introduced as the fitness function of the genetic algorithm. The fitness error $e_{fit,l}$ is calculated from the deviation of the co- and cross-polarized radiation patterns to those resulting from the shared holographic aperture $\vec{C}_{shared,co,n,l}$ $\vec{C}_{shared,cross,n,l}$, and the mask patterns $\vec{C}_{mask,co,n}$, $\vec{C}_{mask,cross,n}$ (see ③ in Fig. 18). It is worth noting that the radiation patterns of the ideal sub-antennas fulfill the fitness function for all azimuth and elevation angles.

A termination criterion $e_{criterion}$ ensures that the GA is aborted as soon as the fitness value $e_{fit,l}$ falls below this threshold for a certain individual (see ④ in Fig. 18). In case, the termination criterion is not fulfilled, a selection out of the L GA individuals based on their fitness value is made (see ⑤ in Fig. 18). Then, a recombination and a mutation of these selected individuals is processed in order to generate descendants, which are then completely or only partially modified (see ⑥ and ⑦ in Fig. 18).

If the termination criterion is fulfilled ($e_{fit,l} < e_{criterion}$), the individual with the optimized holographic multi-feed antenna configuration is found (see ⑧ in Fig. 18). The optimized feeds and hologram offsets determined by the GA computation regarding the minimum radiation pattern error are listed in Table 2. In this antenna design, the closest feeds are placed at a distance of $1.35\lambda_0 = 5.40$ mm, and the diameter of the SWL patch equals $d_{SWL} = 2.05$ mm. Thus, the requirements of (5) are fulfilled.

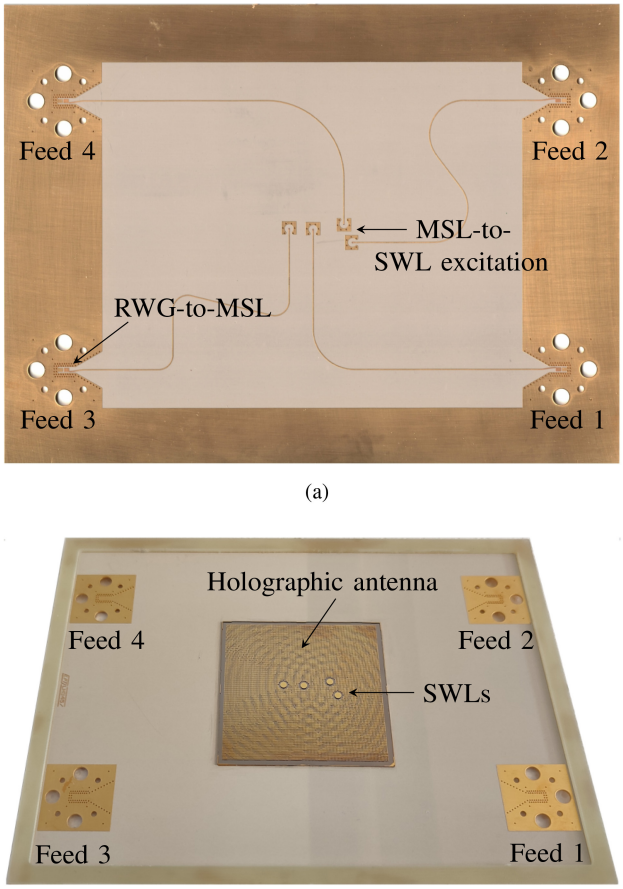

FIGURE 19. Bottom (a) and top view (b) of the manufactured antenna system consisting of the multi-layer feeding network and the holographic multi-feed antenna fixed on the top layer.

V. REALIZATION AND MEASUREMENTS

The holographic multi-feed antenna prototype was fabricated on a fused silica wafer with a relative permittivity of $\varepsilon_r = 3.78$ and a dielectric losses tangent of $\tan\delta = 0.001$. The metallization for the shared holographic aperture and the ground plane consists of a 10 nm thick chromium seed layer, on which a 350 nm gold layer is sputtered. The individual pixel structures are realized by a conventional wet etching process with maximum tolerances of up to 2 µm. The antenna prototype is fixed on a multi-layer feeding structure to provide the excitation of each SWL as depicted in Fig. 19. The bottom view of the feeding structure (see Fig. 19(a)) shows the rectangular waveguide (RWG)-to-microstrip-line (MSL) transition in order to excite the feeding network from the bottom side. The MSL of each feed is connected to a via transition, transforming the horizontal quasi-transverse

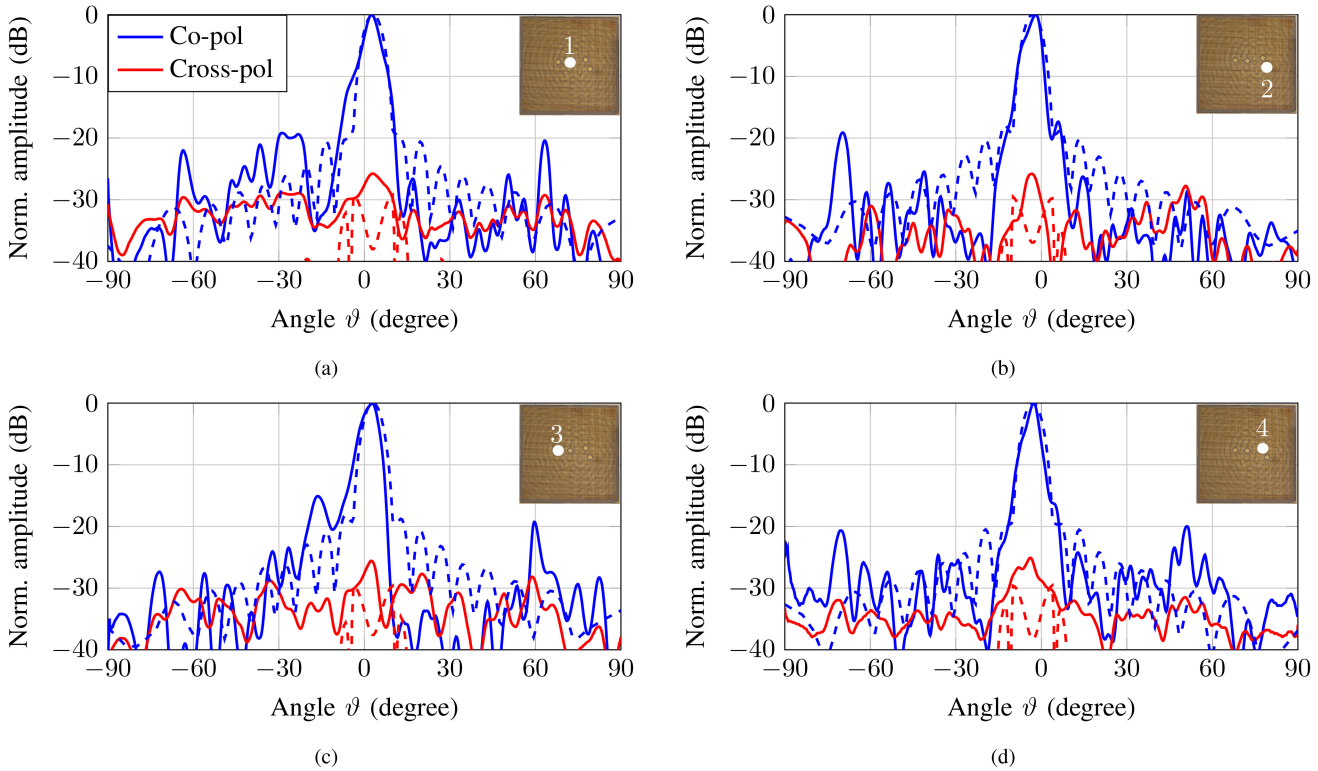

FIGURE 20. Measured (solid line) and simulated (dashed line) radiation pattern of each feed of the holographic multi-feed antenna having four feeds computed by the GA at 77 GHz. (a)-(b) feed 1 and feed 2 at $\phi_0 = 45°$ and (c)-(d) feed 3 and feed 4 at $\phi_0 = 135°$. In the sub-figures, the active feed is highlighted in white.

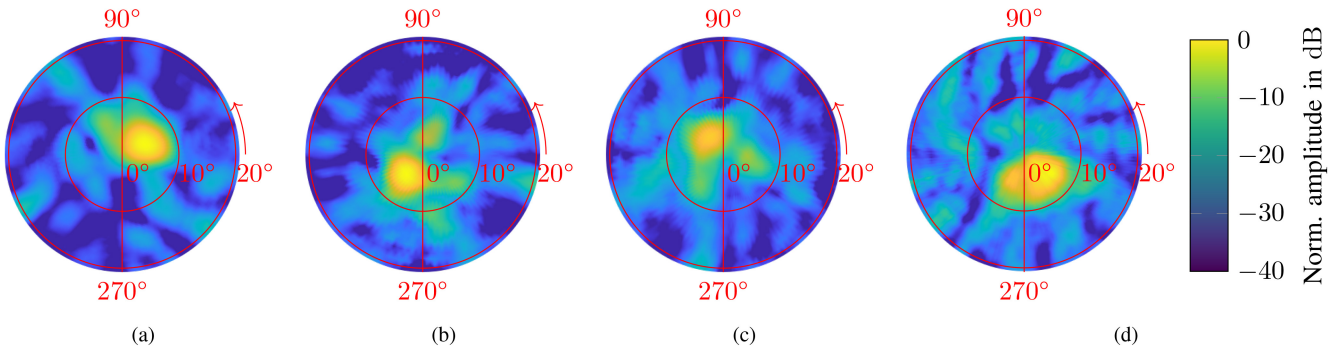

FIGURE 21. Measured 3D-radiation patterns of the holographic multi-feed antenna using glass technology at 77 GHz. (a) feed 1 (b) feed 2 (c) feed 3 and (d) feed 4.

electromagnetic (quasi-TEM) wave propagation into a vertical wave guidance through the multi-layer PCB. In Fig. 19(b) the top view of the multi-layer feeding network can be seen, where the vertical wave propagation enables the SWL excitation for each feed of the holographic antenna. The whole antenna system with the fixed holographic multi-feed antenna on the top layer of the feeding network is depicted in Fig. 19(b). The bottom of the fused silica wafer consists of a fully metallized ground layer, which only has a circular recess at each feed position with a diameter of 600 µm. The footprint of the holographic antenna area on the top layer of the feeding structure ensures an accurate alignment and fixation of the holographic antenna, so that the circular recesses on the bottom side of the antenna fit with the SWL structures of each feed. To reinforce the stability of the antenna system prototype, an additional FR4 frame is glued onto the edges. The MSLs on the bottom side of the feeding network (see Fig. 19(a)) have an identical electrical length. This allows a simultaneous excitation of any number of available feeds as well as the stimulation of each feed individually by a RWG from the bottom side. Thus, the feeding structure has no parasitic impact on the radiation pattern of the holographic antenna. The measurements of the holographic multi-feed antenna have been performed in an anechoic chamber. In Fig. 20 the measured co-polarization (—) and cross-polarization (—) radiation patterns of all four feeds are illustrated in (a)-(d) for elevation angles in the range ±90° at 77 GHz. The four beams are tilted pairwise in the azimuth plane to the angles 45° and 135°. In each case, only one single feed is excited. The co-polarized component of all radiation patterns is primarily inside their fitness mask, and a SLL below 20 dB across

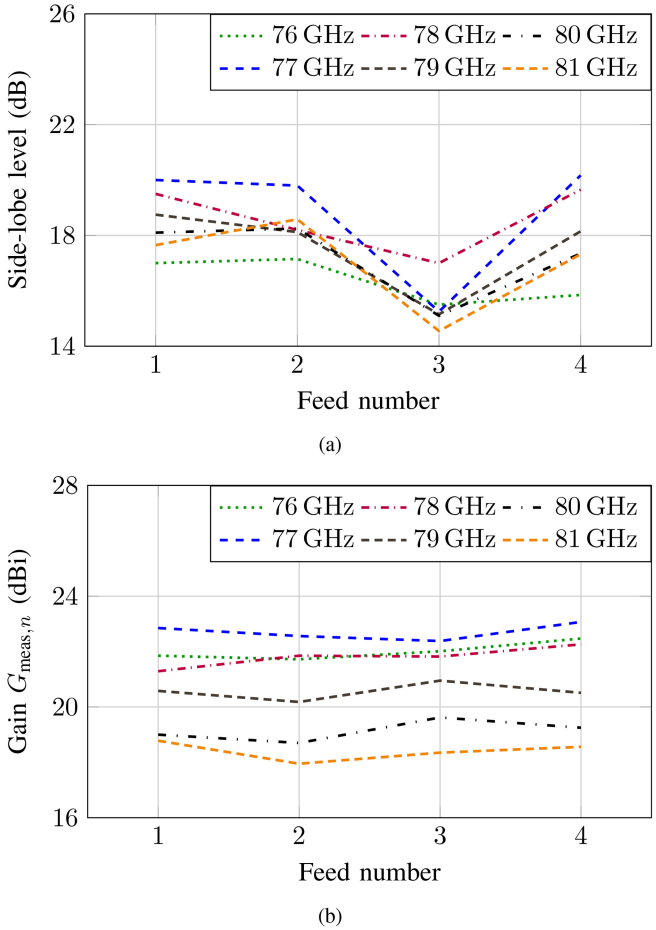

FIGURE 22. Measured side-lobe level (a) and measured antenna gain (b) for all four individual feeds of the holographic multi-feed antenna across the operation frequency range from 76 GHz to 81 GHz.

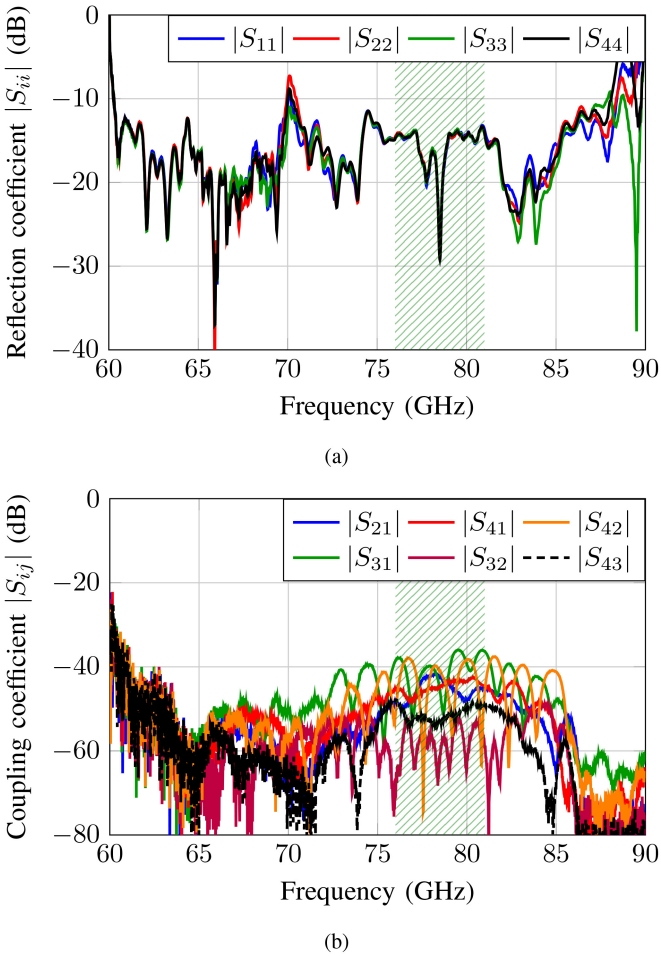

FIGURE 23. Measured S-parameters for all four feeds vs. frequency from 60 GHz to 90 GHz. (a) reflection coefficient (w/o spurious reflections from the env.) (b) inter-port coupling coefficient. highlights the operation frequency range of 76 GHz – 81 GHz.

the whole spherical angle range can be obtained. A notable discrepancy between the mask and the co-polarization is only observed for feed 3 (Fig. 20(c)), where an undesired side-lobe appears, which originates from the process tolerances. The measured peak gain of the holographic multi-feed antenna equals 23.07 dBi at feed 4 and is slightly lower than the analytical gain. This results from the influence of the input reflection coefficient, which is not considered in the analytical gain calculation, and further by the ohmic losses in the metal and dielectric losses of the antenna. The maximum gain imbalance between all feeds equals merely 0.7 dB at 77 GHz. The cross-polarized component of all radiation patterns coincides very well with the fitness mask, and a polarization purity of at least 26 dB is present. This is a bit lower compared to the analytical expectation due to wet etching process tolerances. Overall, the radiation patterns show an excellent agreement between the measured and simulated results. The beam efficiency η_B [26] is a key parameter in the antenna design, as well as the array taper efficiency η_T (ATE). The ATE denotes the influence of the amplitude taper function from (2) on the aperture efficiency of the antenna whereas the beam efficiency presents the antenna gain of each feed normalized to the maximum antenna gain of a uniform electric aperture field distribution [26]. In case of the manufactured antenna system from Fig. 19, a beam efficiency of at least $\eta_B = 56.13\,\%$ and an ATE of $\eta_T = 79.56\,\%$ is achieved. The aperture efficiency η_A of each radiation pattern is about 21 % taking the losses from the MSL-to-SWL transition into account. Furthermore, the performance of the holographic multi-feed antenna prototype has also been verified using a robot-supported mm-wave test range [33]. In Fig. 21 the measured 3D-radiation patterns of all four feeds are depicted across the whole azimuth plane and for elevation angles of ±20° at 77 GHz. The shape of the main beams and the side-lobe suppression are very well-defined in all azimuth planes for each feed. Furthermore, the measured SLL and measured gain of all feeds across the operation frequency range (76 GHz – 81 GHz) are shown in Fig. 22(a) - Fig. 22(b). The highest measured gain for all four feeds is at the design frequency of 77 GHz with a maximum gain imbalance of 0.7 dB and a minimum SLL of 15 dB from feed 3 at 81 GHz is obtained. The lowest gain amounts 18 dBi at feed 2 at 81 GHz. As the holographic

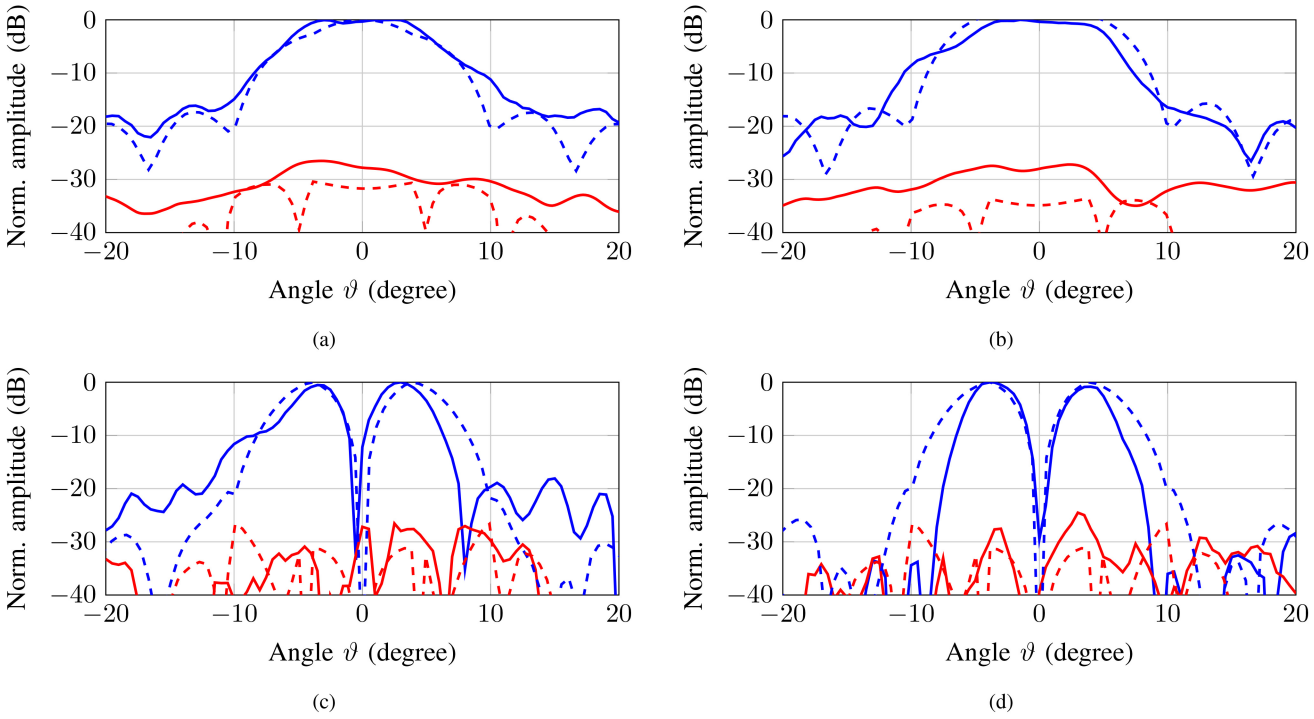

FIGURE 24. Measured (solid line) and simulated (dashed line) sum (a)-(b) and differential (c)-(d) radiation patterns of the 2D-holographic monopulse antenna at 77 GHz, (a) $\phi_0 = 45°$ (b) $\phi_0 = 135°$ (c) $\phi_0 = 45°$ (d) $\phi_0 = 135°$.

antenna scan as a function of frequency in the elevation plane [1], the gain decreases with increasing frequency. At the lower edge of the operation frequency range (76 GHz), the gain is reduced since the impedance of the pixels within the UCs also changes over frequency, and a deviation compared to the impedance surface at 77 GHz occurs. Figure 23 shows the measured S-parameters across the E-band from 60 GHz to 90 GHz. The input reflection coefficient of each feed is depicted in Fig. 23(a). Within the operation bandwidth a return loss below −14 dB can be determined. Additionally, spurious reflections from the environment have been removed by means of time domain filtering. Both the reflection and inter-port coupling coefficients show a very good agreement for the four feeds, especially in the frequency range of operation between 76 GHz and 81 GHz. The inter-port coupling coefficient among the feeds i and j ($i \neq j$) is presented in Fig. 23(b). Within the operation frequency range, a maximum inter-port coupling coefficient between the feeds of −38 dB is obtained.

Each feed of the feeding network is designed with an identical relative phase from the RWG to the SWL excitation. This enables a simultaneous phase-synchronous excitation of all 4 feeds. Thus, the generation of three distinct radiation patterns, namely a sum pattern ($\sum$), a differential-elevation pattern (Δ_{el}), and a differential-azimuth pattern (Δ_{az}) is possible. All the measured beam patterns in Fig. 24 have been normalized to their maxima. The azimuth cuts at 45° and 135° of the measured sum pattern (see Fig. 24(a) and 24(b)) provide a SLL of at least 18 dB below the pattern maxima. A measured polarization purity of at least 28 dB and an antenna

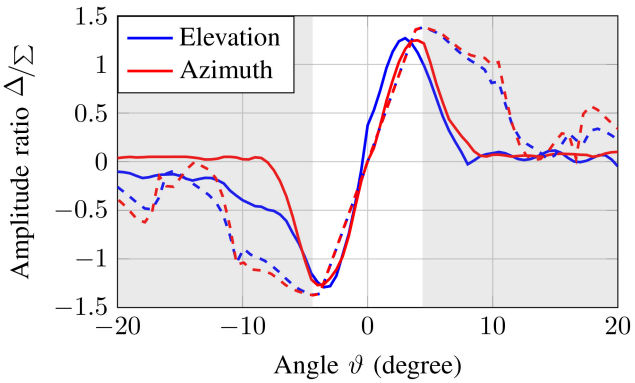

FIGURE 25. Measured (solid line) and simulated (dashed line) amplitude ratio of the 2D-monopulse antenna at 77 GHz.

gain of 26 dBi are achieved resulting in an aperture efficiency for the sum beam of 45 %. The measured differential patterns (see Figs. 24(c) and 24(d)) exhibit good symmetry of the two specular beams, the symmetry is more evident in the Δ_{az}-pattern than in the Δ_{el}-pattern. This probably originates from a small misalignment of the relative phase between the feeds in the manufactured antenna system. In both the Δ_{az}- and Δ_{el}-diagrams a null depth of −30 dB is obtained. The amplitude ratio $\Delta/\sum$ influences the quality of the angle estimation, when integrated into a radar system, which improves as the slope of the curve decreases. Likewise, the unambiguousness and the FoV of the angle estimation is determined by the amplitude ratio. In Fig. 25 the amplitude ratio of the holographic multi-feed antenna prototype is presented, and a FoV of 10° can be determined. As the holographic

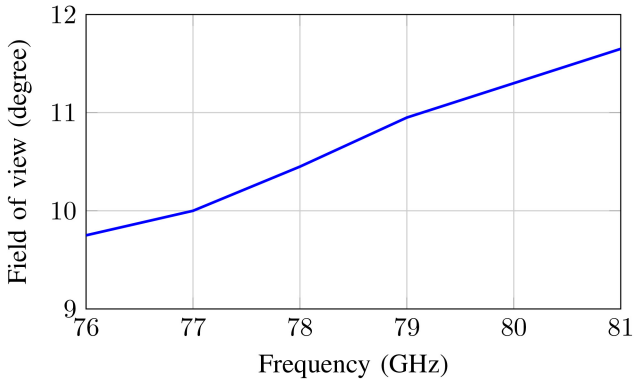

FIGURE 26. Measured field of view of the holographic 2D-monopulse antenna across the operation frequency range of 76 GHz – 81 GHz.

antenna scan as a function of frequency, the FoV increase across the operation frequency as depicted in Fig. 26 and a minimum FoV of 9.75° can be obtained at 76 GHz. Overall, a very good agreement between the measured and simulated radiation patterns and amplitude ratios are present.

VI. CONCLUSION

In this paper a novel holographic multi-feed antenna, realized on a fused silica wafer, for an exemplary integration into a 2D-monopulse radar has been presented. The holographic antenna design is based on a novel multi-feed hologram synthesis method, in which all the sub-holograms are combined onto a single shared holographic aperture by including the angular-dependency of the SW w.r.t. the UC. In order to physically realize the impedance tensors, a novel eigenvector approach is presented. The antenna prototype has four feeds, each of them provides an independent radiation pattern. The four sub-holograms are combined into an optimized shared holographic aperture by using a genetic algorithm. For this purpose, a 3D-radiation pattern mask is applied as the fitness function for each feed in order to find the optimal antenna configuration. The holographic multi-feed antenna was realized on a fused silica wafer and is fixed on a multi-layer feeding network, providing a phase-synchronous excitation of each SWL. The far field measurements of the holographic antenna system prove high-quality radiation patterns for each feed. A peak gain of 23.07 dBi, a side-lobe level of at least 20 dB for feed 1, 2, 4 and 15 dB for feed 3 respectively, and a polarization purity of more than 26 dB at 77 GHz are achieved. This corresponds to beam efficiency of 56.13 % and an ATE of 79.56 %. The aperture efficiency for each beam is about 21 %, whereas for the sum beam 45 % has been reported. The measured gain from 76 GHz to 81 GHz provides a maximum gain imbalance between the four patterns of only 0.7 dB, respectively. The S-parameters of the holographic antenna system were measured across the E-band from 60 GHz to 90 GHz, where an input reflection coefficient below −14 dB and a maximum inter-port coupling coefficient between the feeds of −38 dB is achieved. Furthermore, the radiation characteristics for the 2D-monopulse radar application were successfully verified by measuring the sum pattern, differential pattern in both the elevation and the azimuth planes of the holographic multi-feed antenna system. The amplitude ratio provides a FOV of $9.75° - 11.65°$ from 76 GHz to 81 GHz, the differential beams show a null depth of 30 dB, and the sum beam has a gain of 26 dBi.

ACKNOWLEDGMENT

The authors would like to thank to Norbert Ambrosius from LPKF Laser & Electronics AG for processing and machining the glass wafer to realize the holographic multi-feed antenna prototype.

REFERENCES

[1] T. Frey, A. Dürr, C. Waldschmidt, and T. Chaloun, "Holographic conical beam scanning antenna for mm-Wave radars using glass technology," in *Proc. 51st Eur. Microw. Conf. (EuMC)*, 2022, pp. 825–828.
[2] G. Minatti, F. Caminita, M. Casaletti, and S. Maci, "Leaky wave circularly polarized antennas based on surface impedance modulation," in *Proc. Conf. ICECom 20th Int. Conf. Appl. Electromagn. Commun.*, 2010, pp. 1–4.
[3] G. Minatti, F. Caminita, E. Martini, M. Sabbadini, and S. Maci, "Synthesis of modulated-metasurface antennas with amplitude, phase, and polarization control," *IEEE Trans. Antennas Propag.*, vol. 64, no. 9, pp. 3907–3919, Sep. 2016.
[4] M. Bodehou, E. Martini, S. Maci, I. Huynen, and C. Craeye, "Multibeam and beam scanning with modulated metasurfaces," *IEEE Trans. Antennas Propag.*, vol. 68, no. 3, pp. 1273–1281, Mar. 2020.
[5] M. Döring, T. Frey, C. Waldschmidt, and T. Chaloun, "High-gain holographic multi-feed antenna," in *Proc. 14th German Microw. Conf. (GeMiC)*, 2022, pp. 1–4.
[6] D. J. Hoppe and Y. Rahmat-Samii, *Impedance Boundary Conditions in Electromagnetics*. Washington, DC, USA: Taylor & Francis, 1995.
[7] R. Feger, A. Hamidipour, and A. Stelzer, "Integrated mm-Wave sensors in a package," in *Proc. Asia–Pac. Microw. Conf. (APMC)*, 2013, pp. 209–211.
[8] J. Seo et al., "Miniaturized dual-band broadside/endfire antenna-in-package for 5G smartphone," *IEEE Trans. Antennas Propag.*, vol. 69, no. 12, pp. 8100–8114, Dec. 2021.
[9] W. Wan, Y. Zheng, L. Cao, T. Ye, and Q. Wang, "Low-profile broadband metasurface antenna for 5G antenna-in-package application," in *Proc. IEEE 71st Electron. Compon. Technol. Conf. (ECTC)*, 2021, pp. 1732–1737.
[10] Y. Zheng, W. Wan, Q. Wang, and L. Cao, "Research on integrated metasurface lens for high gain multibeam system in package application," in *Proc. 22nd Int. Conf. Electron. Packag. Technol. (ICEPT)*, 2021, pp. 1–5.
[11] T. Galler, T. Frey, C. Waldschmidt, and T. Chaloun, "High-gain millimeter-wave holographic antenna in package using glass technology," *IEEE Antennas Wireless Propag. Lett.*, vol. 19, no. 12, pp. 2067–2071, Dec. 2020.
[12] T. Jaeschke, C. Bredendiek, and N. Pohl, "A 240 GHz ultra-wideband FMCW radar system with on-chip antennas for high resolution radar imaging," in *Proc. IEEE MTT-S Int. Microw. Symp. Dig. (MTT)*, 2013, pp. 1–4.
[13] M. Hitzler, P. Grüner, L. Boehm, W. Mayer, and C. Waldschmidt, "On monostatic and bistatic system concepts for mm-Wave radar MMICs," *IEEE Trans. Microw. Theory Techn.*, vol. 66, no. 9, pp. 4204–4215, Sep. 2018.
[14] S. Maci, G. Minatti, M. Casaletti, and M. Bosiljevac, "Metasurfing: Addressing waves on impenetrable metasurfaces," *IEEE Antennas Wireless Propag. Lett.*, vol. 10, pp. 1499–1502, 2011.
[15] M. Bosiljevac, M. Casaletti, F. Caminita, Z. Sipus, and S. Maci, "Non-uniform metasurface Luneburg lens antenna design," *IEEE Trans. Antennas Propag.*, vol. 60, no. 9, pp. 4065–4073, Sep. 2012.
[16] R. Quarfoth and D. Sievenpiper, "Artificial tensor impedance surface waveguides," *IEEE Trans. Antennas Propag.*, vol. 61, no. 7, pp. 3597–3606, Jul. 2013.

[17] M. Mencagli, C. D. Giovampaola, and S. Maci, "A closed-form representation of isofrequency dispersion curve and group velocity for surface waves supported by anisotropic and spatially dispersive metasurfaces," *IEEE Trans. Antennas Propag.*, vol. 64, no. 6, pp. 2319–2327, Jun. 2016.
[18] E. Martini, M. Mencagli, D. González-Ovejero, and S. Maci, "Flat optics for surface waves," *IEEE Trans. Antennas Propag.*, vol. 64, no. 1, pp. 155–166, Jan. 2016.
[19] A. Oliner and A. Hessel, "Guided waves on sinusoidally-modulated reactance surfaces," *IRE Trans. Antennas Propag.*, vol. 7, no. 5, pp. 201–208, Dec. 1959.
[20] A. M. Patel and A. Grbic, "A printed leaky-wave antenna based on a sinusoidally-modulated reactance surface," *IEEE Trans. Antennas Propag.*, vol. 59, no. 6, pp. 2087–2096, Jun. 2011.
[21] B. H. Fong, J. S. Colburn, J. J. Ottusch, J. L. Visher, and D. F. Sievenpiper, "Scalar and tensor holographic artificial impedance surfaces," *IEEE Trans. Antennas Propag.*, vol. 58, no. 10, pp. 3212–3221, Oct. 2010.
[22] G. Minatti, F. Caminita, M. Casaletti, and S. Maci, "Spiral leaky-wave antennas based on modulated surface impedance," *IEEE Trans. Antennas Propag.*, vol. 59, no. 12, pp. 4436–4444, Dec. 2011.
[23] G. Minatti, S. Maci, P. De Vita, A. Freni, and M. Sabbadini, "A circularly-polarized isoflux antenna based on anisotropic metasurface," *IEEE Trans. Antennas Propag.*, vol. 60, no. 11, pp. 4998–5009, Nov. 2012.
[24] G. Minatti et al., "Modulated metasurface antennas for space: Synthesis, analysis and realizations," *IEEE Trans. Antennas Propag.*, vol. 63, no. 4, pp. 1288–1300, Apr. 2015.
[25] D. González-Ovejero, C. Jung-Kubiak, M. Alonso-delPino, T. Reck, and G. Chattopadhyay, "Design, fabrication and testing of a modulated metasurface antenna at 300 GHz," in *Proc. 11th Eur. Conf. Antennas Propag. (EUCAP)*, 2017, pp. 3416–3418.
[26] D. González-Ovejero, G. Minatti, G. Chattopadhyay, and S. Maci, "Multibeam by metasurface antennas," *IEEE Trans. Antennas Propag.*, vol. 65, no. 6, pp. 2923–2930, Jun. 2017.
[27] D. González-Ovejero, G. Minatti, E. Martini, G. Chattopadhyay, and S. Maci, "Shared aperture metasurface antennas for multibeam patterns," in *Proc. 11th Eur. Conf. Antennas Propag. (EUCAP)*, 2017, pp. 3332–3335.
[28] D. González-Ovejero, G. Minatti, M. Faenzi, F. Caminita, E. Martini, and S. Maci, "Shared-aperture modulated metasurface antennas," in *Proc. XXXIInd Gen. Assembly Sci. Symp. Int. Union Radio Sci. (URSI GASS)*, 2017, pp. 1–3.
[29] M. Faenzi et al., "A metasurface radar monopulse antenna," *IEEE Trans. Antennas Propag.*, vol. 70, no. 4, pp. 2571–2579, Apr. 2022.
[30] T. Frey, M. Döring, C. Waldschmidt, and T. Chaloun, "Towards holographic antenna systems for MIMO radar and communication applications," in *Proc. 16th Eur. Conf. Antennas Propag. (EuCAP)*, 2022, pp. 1–5.
[31] G. Minatti, F. Caminita, E. Martini, and S. Maci, "Flat optics for leaky-waves on modulated metasurfaces: Adiabatic Floquet-wave analysis," *IEEE Trans. Antennas Propag.*, vol. 64, no. 9, pp. 3896–3906, Sep. 2016.
[32] M. Skolnik, *Radar Handbook*, 3rd ed. New York, NY, USA: McGraw-Hill, 2008.
[33] L. Boehm, F. Boegelsack, M. Hitzler, and C. Waldschmidt, "The challenges of measuring integrated antennas at millimeter-wave frequencies," *IEEE Antennas Propag. Mag.*, vol. 59, no. 4, pp. 84–92, Aug. 2017.

THOMAS FREY (Graduate Student Member, IEEE) received the M.Sc. degree in electrical engineering from Ulm University, Ulm, Germany, in 2019, where he is currently pursuing the Ph.D. degree. From 2017 to 2019, he was a student Trainee with Hensoldt Sensors, Ulm. In 2017, he joined the Institute of Microwave Engineering, Ulm University. His current research interests include holographic multi-feed antennas and planar antenna arrays using glass technology, millimeter-wave radar systems with focus on automotive MIMO radars, and multi-layer PCB structures, all at millimeter-wave frequencies.

MAXIMILIAN DÖRING received the M.Sc. degree in electrical engineering from Ulm University, Ulm, Germany, in 2021, where he is currently pursuing the Ph.D. degree. In 2021, he joined the Institute of Microwave Engineering, Ulm University. His current research interests include holographic antennas, reconfigurable phased arrays, and multilayer antenna systems at millimeter-wave frequencies.

NICO RIESE (Graduate Student Member, IEEE) received the M.Sc. degree in electrical engineering from Ulm University, Ulm, Germany, in 2022, where he is currently pursuing the Ph.D. degree with the Institute of Microwave Engineering. His current research interests include novel waveguide and passive transition structures as well as antenna concepts applicable for multiband radar systems in the micro- and millimeter-wave range.

CHRISTIAN WALDSCHMIDT (Fellow, IEEE) received the Dipl.-Ing. (M.S.E.E.) and the Dr.-Ing. (Ph.D.E.E.) degrees from the University Karlsruhe, Karlsruhe, Germany, in 2001 and 2004, respectively. From 2001 to 2004, he was a Research Assistant with the Institut für Höchstfrequenztechnik und Elektronik, Universität Karlsruhe. Since 2004, he has been with Corporate Research and Chassis Systems, Robert Bosch GmbH. He was heading different research and development teams in microwave engineering, RF-sensing, and automotive radar. In 2013, he returned to Academia and was appointed as the Director of the Institute of Microwave Engineering, Ulm University, Ulm, Germany, as a Full Professor. He authored or coauthored more than 200 scientific publications and more than 20 patents. His research interests include focus on radar and RF-sensing, mm-wave and submillimeter-wave engineering, antennas and antenna arrays, and RF and array signal processing. He has been the co-recipient of 12 best paper awards since 2014. He was the Chair of the IEEE MTT-27 Technical Committee on wireless enabled automotive and vehicular applications. He was the Two-Time TPC Chair and the General Chair of the IEEE MTT International Conference on Microwaves for Intelligent Mobility. Since 2018, he has been an Associate Editor for IEEE MICROWAVE WIRELESS COMPONENTS LETTERS. He is a reviewer for multiple IEEE transactions and many IEEE conferences in the field of microwaves. He is a member of the Executive Committee Board of the German MTT/AP Joint Chapter and the German Information Technology Society.

TOBIAS CHALOUN (Member, IEEE) received the Dipl.-Ing. and Dr.-Ing. degrees (Hons.) in electrical engineering from the University of Ulm, Ulm, Germany, in 2010 and 2016, respectively. From 2010 to 2016, he was a Research Assistant with the Institute of Microwave Engineering, Ulm University, where he conducted his doctoral studies in the field of highly integrated antenna systems for communication applications at millimeter wave frequencies. Since January 2017, he has been a Senior Researcher and a Lecturer with the Institute of Microwave Engineering. His main research interest concerns multilayer antennas and circuits, millimeter-wave packaging and interconnects, phased array antenna systems, and millimeter-wave radar sensors. He has been awarded for the Best Paper in the IET Microwaves, Antennas and Propagation in 2016. He was the recipient of the Best Paper Award at the German Microwave Conference in 2015. He currently serves as a reviewer for multiple IEEE journals and conferences. He is a member of the European Microwave Association and the Institute of Electrical and Electronics Engineers and a Founding Member of the IEEE MTT-S Technical Committee 29 on Microwave Aerospace Systems.